

Geometrical and energy scaling in the plasma generated during laser ablation of FeSe

S. B. Harris^{a,*}, C. W. Cotton^a, R. R. Arslanbekov^b, R. P. Camata^a

^aDepartment of Physics, University of Alabama at Birmingham, Birmingham, Alabama 35294, USA

^bCFD Research Corporation, Huntsville, Alabama, 35806, USA

Abstract

FeSe monolayers benefit from enhanced superconductivity when interfaced with SrTiO₃. With a dawning understanding of the underlying mechanisms of T_c enhancement, synthesis of new monolayer FeSe interfaces or heterostructures with different materials enables deliberate control or design of quantum properties. Pulsed laser deposition (PLD) allows the rapid synthesis of FeSe heterostructures with a wide variety of material systems, provided that the properties of the laser-produced plasma can be correctly tuned for monolayer growth. In this article, we show how the most important plasma parameters for film growth, density and kinetic energy, can be fine-tuned to promote high quality monolayer growth. We report comprehensive Langmuir probe measurements during the laser ablation of FeSe and introduce the first 2D-axisymmetric simulation capable of accurate results at the length and time scales relevant for PLD. Spatially resolved measurements of the time-of-flight kinetic energy distribution reveal that the number of highly energetic particles increases as the plasma expansion progresses in high vacuum. Decreasing the laser spot size on the target with a constant fluence reduces the plasma density by 2 orders of magnitude and reduces the number of high energy particles in the plume. Thus, by choosing a small laser spot size and using a laser energy below the plasma absorption threshold, a low density, low kinetic energy plume can be created, without the aid of a background gas, to promote monolayer growth of FeSe.

Keywords: Monolayer FeSe, Laser ablation, Laser generated plasma, Pulsed laser deposition diagnostics, 2D materials

1. Introduction

Growth of FeSe thin films and monolayers has been of great interest since the discovery of its interface enhanced superconductivity [1]. The superconducting gap of monolayer FeSe on SrTiO₃ (STO) is increased by a combination of electron doping of the FeSe layer and forward-scattering, electron-phonon interactions at the interface with STO [2]. Moreover, monolayer FeSe exhibits a giant thermoelectric response that arises concomitantly with high T_c on STO [3] and shows enhanced T_c on MgO via the application of an electric field [4]. Because of the combination of electronic and interface induced mechanisms that lead to the enhancement of T_c , FeSe is an excellent laboratory for the exploration of out-of-equilibrium and interface enhanced phenomena and may be a highly versatile and multifunctional material for devices.

The heterostructuring of FeSe monolayers with different material systems in layered or superlattice structures is a promising approach to uncover new control mechanisms over the quantum properties of FeSe [5]. Such heterostructuring also provides a shield for the delicate monolayers from the ambient environment. Pulsed laser deposition (PLD) allows the rapid synthesis of monolayer FeSe heterostructures with a variety of substrates, interlayers, and capping materials, representing numerous opportunities to explore complex FeSe-based systems.

Growth of monolayer materials by PLD is a developing field and requires exquisite control over the properties of the laser-produced plasma plume. The density and kinetic energy distribution affect the crystallinity, growth mode, and defect concentration of the resulting films. Deliberate control of the properties of the plasma opens new synthesis opportunities for the growth or modification of ultra-thin, FeSe-based heterostructures that complement the typical crystal growth approach of molecular beam epitaxy.

Correlations between film characteristics and PLD parameters have been made numerous times but are largely empirical [6, 7, 8, 9, 10]. In this paper, we provide a quantitative explanation of how specific laser parameters affect the plasma through detailed electrical probe measurements. Recent success in the synthesis of 2D materials and very high quality perovskites by PLD rely heavily on the understanding of the plume dynamics. For example, since the formation energy of an O vacancy in SrTiO₃ films is 0.5 eV [11], SrTiO₃ films are traditionally grown in a narrow range of oxygen background pressure (≈ 100 mTorr) and laser fluence to maintain stoichiometry [12]. Recently, defect free SrTiO₃ films were grown in high vacuum by using an in-situ ion probe to monitor the kinetic energy of the plume [13]. In another study aided by plasma measurements, further reduction of plume kinetic energy by ablating a GaSe target in 1 Torr of Ar background gas showed the successful growth of 1-3 layer nanosheets [14]. Since the binding energy of a monolayer of FeSe to SrTiO₃ has been calculated by DFT to be ~ 0.7 eV [15], attempting to grow monolayer FeSe will re-

*Corresponding author

Email address: sumner@uab.edu (S. B. Harris)

quire similar conditions. Other than introducing a background gas, the ion and plasma properties can be controlled with the laser fluence and energy delivered to the target surface. These parameters can be modified independently by imaging an aperture that is smaller than the original beam area onto the target. The effect is that the laser spot area on the target is decreased proportionally with the energy, while maintaining a constant fluence.

We report comprehensive Langmuir probe measurements of the PLD plasma parameters using an FeSe ablation target in a high vacuum environment. The density of the plasma can span orders of magnitude (10^{18} - 10^{20} m^{-3}) with the same fluence by adjusting the laser spot area/energy on the target. The electron temperature is shown to range from 0.3-5 eV and is related to the number of ions with very high kinetic energy. The kinetic energy distribution of ions can be controlled below the plasma shielding threshold, where the number of highly energetic ions gradually reduces as laser spot size decreases. Precise knowledge of the plasma plume can be used to design future PLD growth experiments of monolayer FeSe.

2. Experimental Details

The FeSe ablation target was synthesized from elemental precursors with the nominal stoichiometry $\text{FeSe}_{0.97}$ using the same technique as reference [8]. This target stoichiometry produces the highest T_c in thick FeSe films. Properties of the plasma produced from the target were measured with Langmuir probes of two different geometries. The PLD system is shown schematically in Fig. 1. A cylindrical probe consisting of a $101.6\text{-}\mu\text{m}$ (32 AWG) radius, 4.5-mm long platinum wire was used to measure plasma parameters. By stepping the probe bias, cylindrical probe theories permit extraction of the electron temperature (T_e) and density (n_e) from the probe current vs. bias voltage characteristics ($I-V_p$) [16]. A 10×10 mm square planar probe composed of a thin molybdenum foil backed with alumina was used for measurements of the time of flight (TOF) distribution of ions. Under strong negative bias, the large probe area can tolerate the high current collected without damage, where the platinum, cylindrical probe quickly melts. Each probe was placed along the direction normal to the surface of the FeSe ablation target and was attached to a linear translation vacuum feedthrough, in order to be positioned at distances between zero and 5.500 ± 0.005 cm from the target. The probes are connected to a bias voltage source and the collected current is determined as a function of time ($I-t$) from the voltage drop across a 10Ω resistor, connected to ground. An oscilloscope was used to average the signal produced by at least 30 laser pulses for each value of probe bias. The target was constantly rotating and was cleaned with 1000 pulses before data collection began. The background pressure was kept at 3×10^{-6} Torr, consistent with typical pressures used in PLD. The KrF laser pulse had a duration of 20 ns and wavelength of 248 nm (Lambda Physik LPX 305i). To change the spot size (energy) on the FeSe target, a rectangular aperture was placed in the beam path prior to passing through the focusing lens. Imaging the aperture changes the size of the focused spot on the target

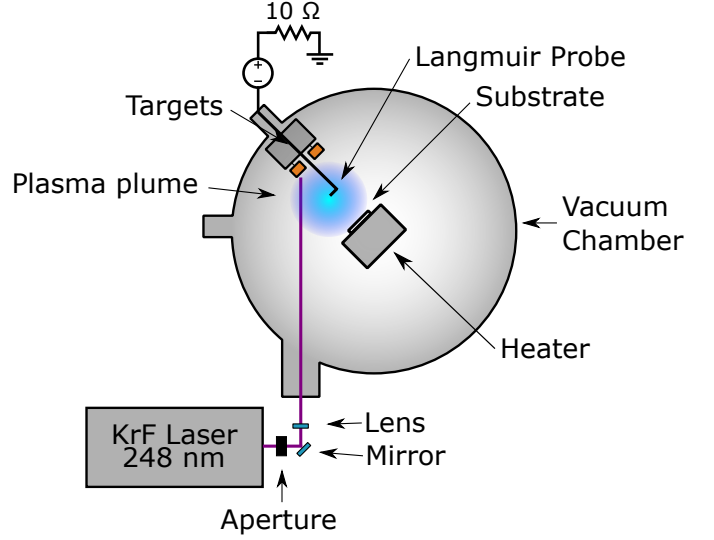


Figure 1: Schematic of the pulsed laser deposition system, including Langmuir probe. A 10×10 mm planar probe is used to acquire ion TOF data, whereas $I - V_p$ characteristics are studied with a $101.6\text{-}\mu\text{m}$ radius (32 AWG) cylindrical probe of length 4.5 mm. Each probe is attached to a micrometric linear translation feedthrough that allows its placement at distances between zero and 5.500 ± 0.005 cm from the target. A rectangular aperture of variable size is placed before the focusing lens to change the spot size on the target while maintaining a fixed energy density.

while maintaining a constant energy density. Energy density was varied by changing the KrF laser voltage with a fixed aperture size.

3. Probe Theories

The density of the plasma is known to be correlated with the growth mode, grain size, and growth rate of thin films [17]. The kinetic energy of the ions primarily affects the resulting crystal structure and plays a role in the formation of defects. As such, these parameters play the most direct role in materials growth by PLD. The more fundamental properties of the plasma, such as electron temperature and Debye length, have not been directly related to material characteristics in PLD studies. The electron temperature during the early formation of the plasma serves to set up an electric field that accelerates positive ions, as will be shown later. The Debye length is needed to choose which Langmuir probe theory can be applied to determine T_e and density. In this section, the probe theory and data analysis methods used to measure the plasma parameters are discussed.

In order to obtain reliable values for the plasma parameters from the $I - V_p$ characteristic curve, the contributions from the ion current I_i and electron current I_e need to be separated. A typical $I - V_p$ characteristic is shown in Fig. 2a. When the probe bias V_p is sufficiently more negative than the space potential V_s , the probe collects the ion saturation current I_{isat} . Conversely, when V_p is much more positive than V_s , the electron saturation current is collected, I_{esat} , which represents the random thermal electron current to the probe. In the region between, the probe current involves contributions from both the ions and electrons.

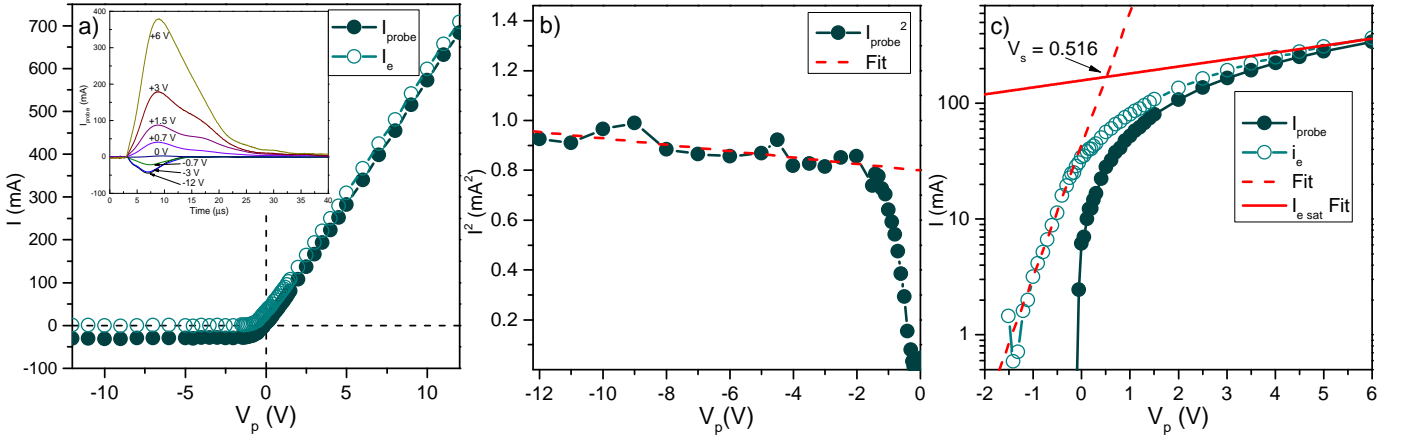


Figure 2: a) $I - V_p$ characteristic before (solid circles, I) and after (open circles, I_e) ion current subtraction. The inset shows the time dependence of probe current for several different values of bias. b) $I^2 - V_p$ in the ion saturation region is fit with OML theory to determine ion/electron density. c) $I - V_p$ characteristic before and after ion current subtraction on a semi-log scale, around the space potential. The linear portion is extended to lower V_p after ion current subtraction and is fit to determine T_e . The electron saturation is also fit to find V_s at the intersection with of the two lines.

The electron current from a Maxwellian electron energy distribution is exponential and is given by Eq. 1 and Eq. 2 [18]:

$$I_e = I_{e,sat} \exp\left(\frac{e(V_p - V_s)}{kT_e}\right) \quad (1)$$

$$I_{e,sat} = \frac{1}{4} en_e A_p \sqrt{\frac{8kT_e}{\pi m_e}} \quad (2)$$

where n_e is the electron density, e is electron charge, A_p is the surface area of the probe, T_e is electron temperature, and m_e is electron mass. The semi-log plot of $\ln(I_e)$ vs V_p produces a straight line below V_s , whose slope yields T_e . Subtraction of the ion current may be done in a variety of ways, with the simplest being to assume that the ion saturation current is not dependent on V_p . If the electron and ion temperature are assumed to be similar, $I_{i,sat}$ has the same form as $I_{e,sat}$, replacing m_e with the ion mass M and T_e with T_i . If $T_i \ll T_e$, $I_{i,sat}$ is given by the Bohm current [19]. Using these methods, typically the most negative value in the ion saturation region is used as the constant value or a simple line is fit and subtracted from the probe data. In practice, this is only valid in a limited set of conditions (laser fluence, target-probe distance, etc.) To account for ion current more accurately across a broader range of conditions, orbital-motion-limited (OML) theory for cylindrical probes is applied. OML theory assumes negligible collisions in the sheath surrounding the probe and as such, the current that the probe collects is limited by the orbital motion of ions around the cylindrical probe and is given by [20, 21]:

$$I_i = A_p n e \frac{\sqrt{2}}{\pi} \left(\frac{e(V_s - V_p)}{M}\right)^{\frac{1}{2}} \quad (3)$$

where $I_i^2 \propto V_p$. While OML theory is most accurate when the ratio of the probe radius to the Debye length $\xi = R_p/\lambda_d < 3$, it is known to provide valid results well outside of this applicability range, even in high density plasmas, and is widely used in industry for a variety of plasma conditions [22]. To even more

accurately correct for the ion current, more complex models such as Allen-Boyd-Reynolds (ABR) or Bernstein-Rabinowitz-Laframboise (BRL) can be used which account for finite plasma sheaths and finite sheaths with orbital motion, respectively. For $3 < \xi < 100$, the real plasma density lies between what is predicted from OML and BRL theories, with OML providing an upper limit. See Chen [21] for an excellent discussion and comparison of these theories. The present study finds the maximum $\xi \approx 140$ so OML will provide a more robust and accurate estimation of n_e and T_e versus simply subtracting the Bohm current, without the complication of ABR or BRL theory.

Each $I - V_p$ curve is treated in the following way. First, a time is chosen from the $I - t$ dataset and the probe current at that time is extracted from all values of probe bias and plotted to construct the $I - V_p$ characteristic. Fig. 2a shows an $I - V_p$ curve on a linear scale before and after ion subtraction, while the inset displays a selection of the $I - t$ curves from which it was constructed. Next, I^2 vs V_p is plotted and a line is fit whose parameters will be used to determine n (imposing quasineutrality, $n_i \approx n_e \approx n$) and I_i and is shown in Fig. 2b. Finally, I_i is subtracted from the raw data and the slope of the exponential portion of I_e vs V_p is fit to determine T_e (Fig. 2c). The intersection of this line with a line drawn through the electron saturation is used to determine the space potential V_s , and this value is used to calculate n . Once n and T_e are determined, the Debye length can be calculated with Eq. 4.

$$\lambda_d = \sqrt{\frac{\epsilon_0 k T_e}{n e^2}} \quad (4)$$

4. Results and Discussion

The probe was placed 55 mm away from the FeSe ablation target along the central axis to obtain plasma parameters at a position that is typical for thin film depositions. An $I - V_p$ characteristic was obtained for 6 different laser spot sizes ranging from 3.5-19.3 mm². With a fixed laser fluence, the concept of

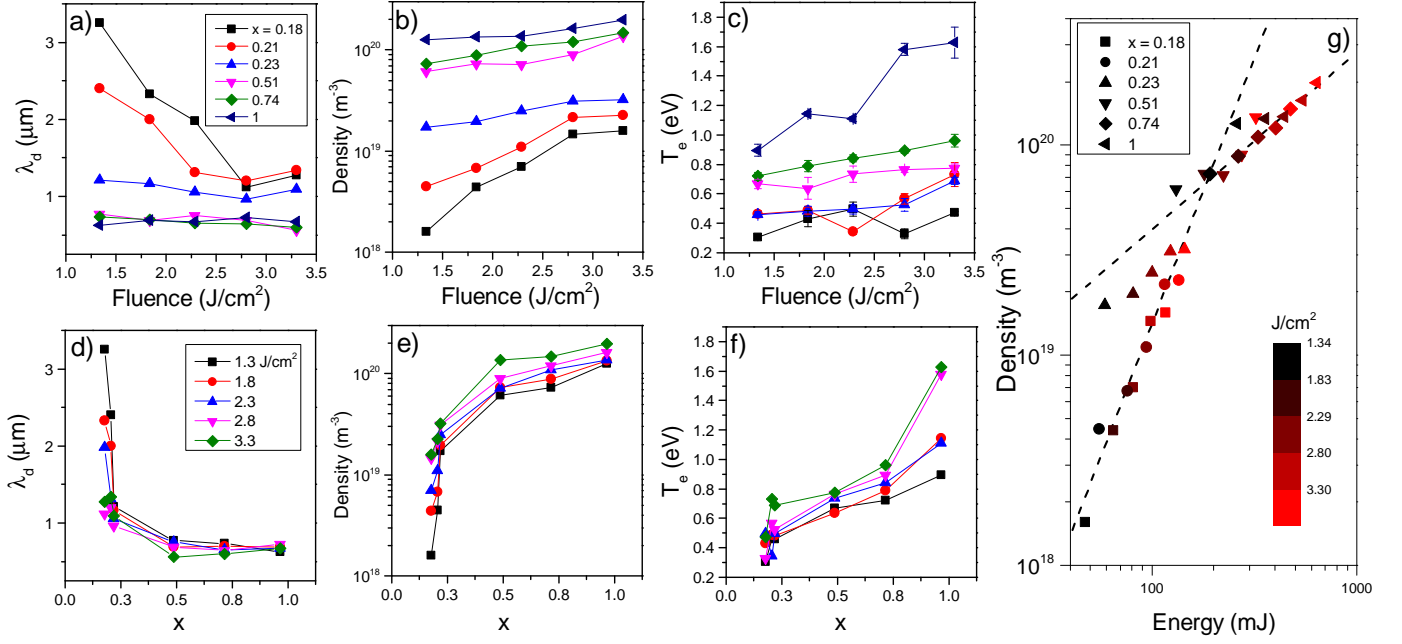


Figure 3: Parameters of the plasma produced from the ablation of the FeSe target, measured at 55 mm from the target surface. The top row shows how the a) Debye length (λ_d), b) density (n), and c) electron temperature (T_e) for different, fixed laser spot sizes varies with fluence. A fractional parameter x is defined here as the ratio of laser energy before and after the aperture (E/E_0) or the ratio of the spot size on the target with and without the aperture (A/A_0), equivalently. T_e and n both increase linearly with increasing fluence, for all x , with a constant λ_d when the energy delivered to the target falls above the plasma absorption threshold. The bottom row, d-f, displays the same data but with fixed laser fluence for various x . While T_e increases gradually with x , n increases by 10^2 rapidly up to a point and then the rate of increase slows, leading to a saturation at small λ_d . Using fluence and spot size to calculate the energy delivered to the FeSe target, g) n versus laser energy shows the universal scaling of density with energy, which displays the plasma absorption threshold near ~ 180 mJ, which is independent of laser fluence.

energy delivered to the target and laser spot size on the target are equivalent. A fractional parameter x is introduced and is defined, equivalently, as the ratio of laser energy before and after the aperture (E/E_0) or the ratio of the spot size on the target with and without the aperture (A/A_0). For each value of x , various fluence was used in the range 1.34-3.30 J/cm². As described in section 3, an $I - V_p$ curve was extracted at the time of maximum ion current, which has previously been shown to be the location of maximum electron temperature [23]. Values of T_e , n , and λ_d were determined for all permutations of x and fluence. Fig. 3a-c shows how these parameters depend on laser fluence, while keeping x fixed. The electron temperature is linear in this range of laser fluence for all x (Fig. 3c). For $x = 0.18$, T_e ranges from 0.31 eV at 1.34 J/cm² to 0.47 eV at 3.3 J/cm². These values are similar to the bulk of PLD plasmas reported in the literature [24] but slightly higher due to shorter distance to the target than most studies. Large values of x produce a much hotter plasma with T_e in the range 0.9-1.6 eV. The density (Fig. 3b) shows a similar trend, existing in a broad range between 1×10^{18} - 1×10^{20} m⁻³ with the highest densities achieved for large x and high fluence. For $x > 0.23$, the ratio of T_e/n remains roughly constant as fluence is increased, which is evident by a constant λ_d shown in Fig 3a with a value of ≈ 0.7 μ m. At $x = 0.23$, λ_d is still approximately constant with laser fluence but with a greater value at ≈ 1 μ m. The two lower values of x show gradual increase towards greater λ_d as fluence decreases, reaching a peak value of 3.25 μ m.

The effect of changing x with a fixed fluence is markedly

different from a fixed x with various fluence, and is shown in Fig. 3d-f. Most notably, the density drops 2 orders of magnitude with decreasing spot size for all of the fluences examined, decreasing much more precipitously than the electron temperature. The result of this unbalanced rate of change between the two parameters is that the Debye length (Fig. 3d) is largest for every value of fluence at small x and rapidly converges to a constant value with increasing x . Projecting these results onto a plot of density vs laser energy (Fig. 3g) for each x displays what could be interpreted as a “kink” at approximately 180 mJ after which the slope decreases. This has been previously attributed as the threshold for plasma absorption of the laser pulse, but was reported in terms of fluence [25]. Since this data was collected with many different values of laser fluence, it is clear that laser energy to the target is the determining factor for plasma absorption of the laser. This means, that for any laser spot size on the target, the fluence threshold is different. Below the threshold, the density decreases at a much greater rate than the temperature, and thus λ_d becomes larger.

The same measurements were repeated with the probe placed 15 mm from the target. The trends that were observed at 55 mm are the same, but the magnitudes of T_e and n are greater. Considering the minimum case of $x = 0.18$ and 1.34 J/cm², $T_e = 0.64$ eV and $n = 1.66 \times 10^{19}$ m⁻³ which represents a significant increase in density and temperature relative to the same conditions at 55 mm. Only the data collected with x up to 0.51 could reliably be analyzed using OML theory, which is evident by a change in the shape of the $I - V_p$ characteristic. Figure 4

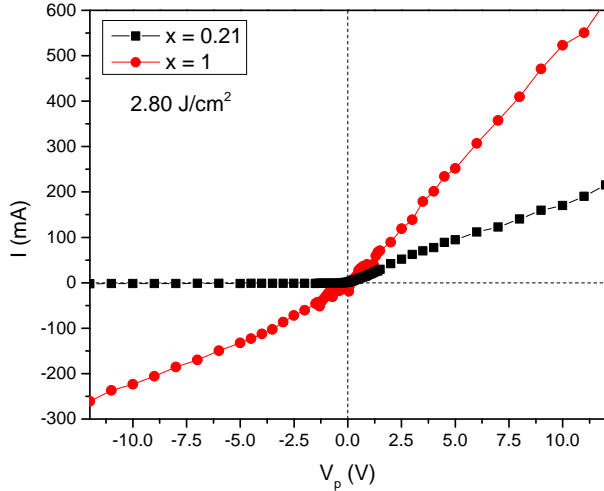


Figure 4: $I - V_p$ characteristics collected at 15 mm from the ablation target. For lower values of x , OML theory may still be used when the probe is close to the target but the ion current contribution becomes too significant as x is increased.

shows two $I - V_p$ curves for 2.8 J/cm^2 collected at 15 mm from the target. The ion current for $x = 0.21$ still follows the $I^2 - V_p$ relationship predicted by OML, with T_e and n of 1.04 eV and $5.15 \times 10^{19} \text{ m}^{-3}$ respectively. With large x , however, the ion current continues to become more negative with with increasingly negative bias and can no longer be fit with OML scaling. For extended studies with Langmuir probes very close to the ablation target, a different probe geometry is needed. A probe with a much smaller radius, perhaps necessarily as small $10 \mu\text{m}$, could be used to maintain $\xi < 100$ in order to apply OML theory but the high currents that would be drawn due to the high densities and the km/s particle flow velocities will heat and damage the probe. More practically, ABR theory could be applied using the same probe to account for the ion current but this is beyond the scope of the present study.

Since density and temperature were measured at two different positions along the central axis of the plasma during the expansion, these quantities can be related by treating the plasma as an ideal gas undergoing isentropic expansion, as is done in many fluid models [26]. For an isentropic process, the temperature and density of two different states are related by the ratio of specific heats, $\gamma = C_p/C_v$, using Eq. 5.

$$\frac{T_2}{T_1} = \left(\frac{n_2}{n_1}\right)^{(\gamma-1)} \quad (5)$$

Using T_e and n for each pair of measurements taken at 15 mm and 55 mm in which OML was applicable (20 pairs), the average ratio of specific heats was determined to be $\gamma = 1.6 \pm 0.11$. This value is close to what is expected of a monatomic ideal gas ($\gamma = 5/3$). Additionally, γ may be used to estimate other quantities through the adiabatic expansion law as well as quantities that may not be available due to experimental limitations. For example, OML was not able to be applied to the the $I - V_p$ curve in Fig. 4 for $x = 1$ to calculate the density. A rudimentary estimation of T_e can be done by using a straight line subtraction of the ion saturation current to estimate $T_e = 5.2 \text{ eV}$. This tem-

perature used as T_1 with T_2 and n_2 taken from the measurement at 55 mm, can be used in Eq. 5 to predict $n = 9.46 \times 10^{20} \text{ m}^{-3}$ at 15 mm. Calculating $\lambda_d = 0.55 \mu\text{m}$ indicates that $\xi = 184$, which is consistent with both the failure of OML for this case and the factor of 10 increase in density that is expected from other measurements. Under high vacuum conditions, we find that γ is independent of laser energy or fluence in the range that was studied. At higher background pressures, into the torr range, γ would be expected to drop as the formation of dimers and trimers begins to occur [27] with the eventual formation of nanoparticles for certain values of x . A study on the ablation of Ag estimated a lower ratio of specific heats, $\gamma = 1.1-1.4$, based on measurements of the expansion velocity off the central axis of the plume and an estimate for initial plasma thickness that fit well to $I - t$ probe measurements [28].

Of particular interest in PLD is the time-of-flight (TOF) kinetic energy distribution of the ions. This distribution can be calculated directly from the $I - t$ traces by a change of variables using Eq. 6 [29] where A is the area of the probe.

$$\frac{dN}{dE} = \frac{I(t)t^3}{Med^2A} \quad (6)$$

First, the TOF distribution was measured at two distances from the target, 15 mm and 55 mm. In Fig. 5a, the most probable kinetic energy (MPKE) at 15 mm away from the target is found to be low, from 1-1.3 eV for the whole range of x . Increasing x leads to a greater number of ions with high kinetic energy, as seen by the long tail out to 22.5 eV. For small x , this tail is much shorter and the kinetic energy is “cut-off” at lower values around 5-10 eV.

At 55 mm away from the target (Fig. 5b), the TOF distribution has evolved to be much more energetic, with the most probable energies centered around $\approx 18 \text{ eV}$ and the high energy tail extending between 50 eV to 100 eV. This behavior is the same for all other values of fluence, with the primary difference being the increase in number of particles. In the case of small x , the absence of a highly energetic tail indicates that the dominate mechanism of sputtering is the primary, thermal one and has been seen in other studies [30] using quadrupole mass spectroscopy. This is consistent with the below-threshold behavior shown in Fig. 3g, since the patent shift in the shape of the distribution aligns with the “kink” at 180 mJ. Similar behavior was reported as a broadening in the FWHM of the ion current vs. time trace collected by a Faraday cup in an older study [31], also by varying x . A different study showed that the velocity distribution of ions broadens with decreasing spot size but the spot size was changed by focusing the laser to a tighter spot and maintaining a fixed laser energy, thus increasing the fluence [32].

To explore the evolution of the TOF distribution, the same measurements were repeated at 1 mm increments from 15-55 mm using $x=0.18$ at 1.34 J/cm^2 . The results are shown in Fig. 6 in a color map of dN/dE as a function of TOF kinetic energy and distance from the target. The MPKE is observed to shift to higher energy as the plasma expands away from the target. The width of the distribution also increases, leading to greater densities of energetic species as distance far from the

target. The velocity of the expansion is constant in high vacuum but the increasing width and drift to higher energy in the distribution can only be explained through some acceleration mechanism. The origin of this dynamic behavior is explained by the presence of an ambipolar electric field at the front of the expansion which accelerates a small percentage of the ions [33]. This electric field is produced by two different populations of electrons which consists of a colder, high density population and a low density, highly energetic tail species that escape from the plasma during its early formation. The resulting charge imbalance creates a strong electric field which slows the energetic electrons to prevent escape and accelerates the ions behind them. The magnitude of the electrostatic potential energy barrier W that forms has been shown to be roughly propor-

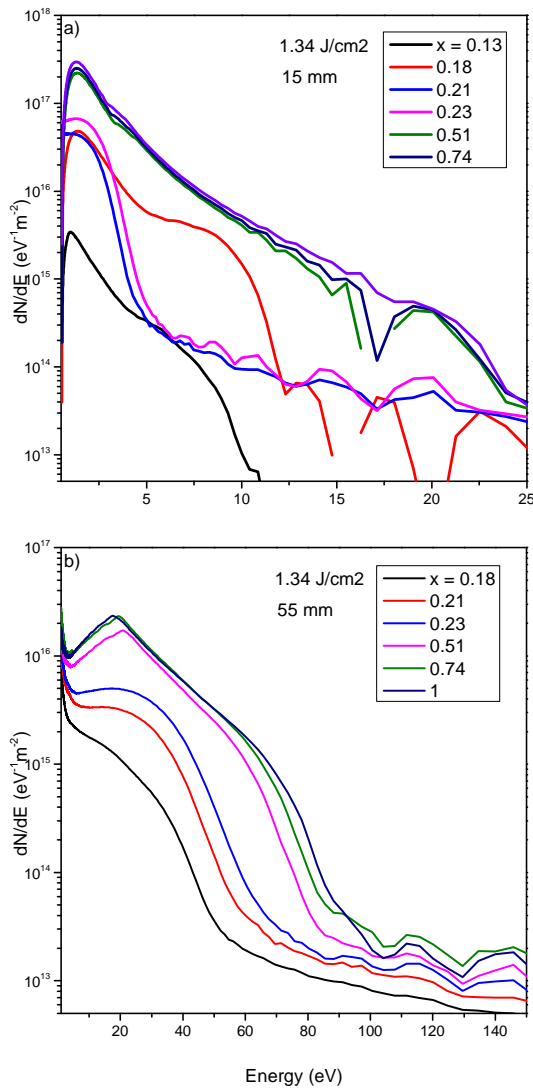


Figure 5: Time of flight kinetic energy distribution, assuming Fe ions, taken at a) 15 mm and b) 55 mm away from the target using the same laser fluence of 1.34 J/cm^2 with different laser spot sizes. Close to the target, the distribution is dominated by the thermal component with few higher energy ions out to 22.5 eV for large x . Farther from the target, a significant portion of the ions have been accelerated by the electric field at the plasma expansion front to high energies extending out to 100 eV.

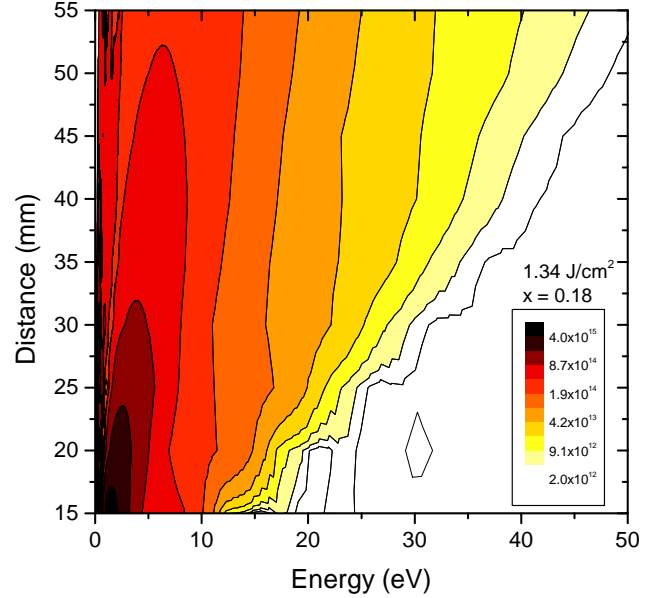


Figure 6: Map of dN/dE as a function of distance from the ablation target and kinetic energy. The most probable energy gradually shifts higher and the distribution becomes more broad as the expansion goes on, leading to more highly energetic species at long distances.

tional to T_e and is $W \approx 30 kT_e$ with the MPKE $\approx Z W$ (which is independent of mass), where Z is ion charge [29]. Applying this formula, at 55 mm from the target using $x = 0.18$ and a laser fluence of 3.3 J/cm^2 , T_e was measured to be 0.47 eV which gives MPKE = 14.1 eV for singly charged ions which is in line with the present findings. Similarly for $x = 0.18$ with 1.34 J/cm^2 , MPKE = 9.3 which also matches well with the experiment. Applying this formula to distributions collected at 15 mm fails since primarily only the thermal ions are detected. Recall that these experiments are done under high vacuum conditions (10^{-6} Torr), this behavior should not be expected at higher pressures since the plasma ions will be scattered and slowed by the background gas.

5. Comparison to Simulations

The experimental results are compared with a simulation of the laser-produced plasma. The laser plasma was simulated using a model that couples laser-induced surface evaporation with fluid plasma expansion. A thorough discussion of the model can be found in a previous publication [34] which outlines the results of a 1D simulation of ablation of a Cu target. Since the model only accounts for four species (neutral, singly and doubly ionized atoms, and electrons for one element) and most of the physical properties required in the model are not available for FeSe, a Cu target will be simulated. This enables comparison with numerous computational studies and experiments of Cu ablation. The results of the simulation can be qualitatively compared to the experimental results for FeSe.

One-dimensional simulations contain no concept of laser spot size. Thus, they are only quantitative when the laser spot is small when compared to the expansion distance. This is is

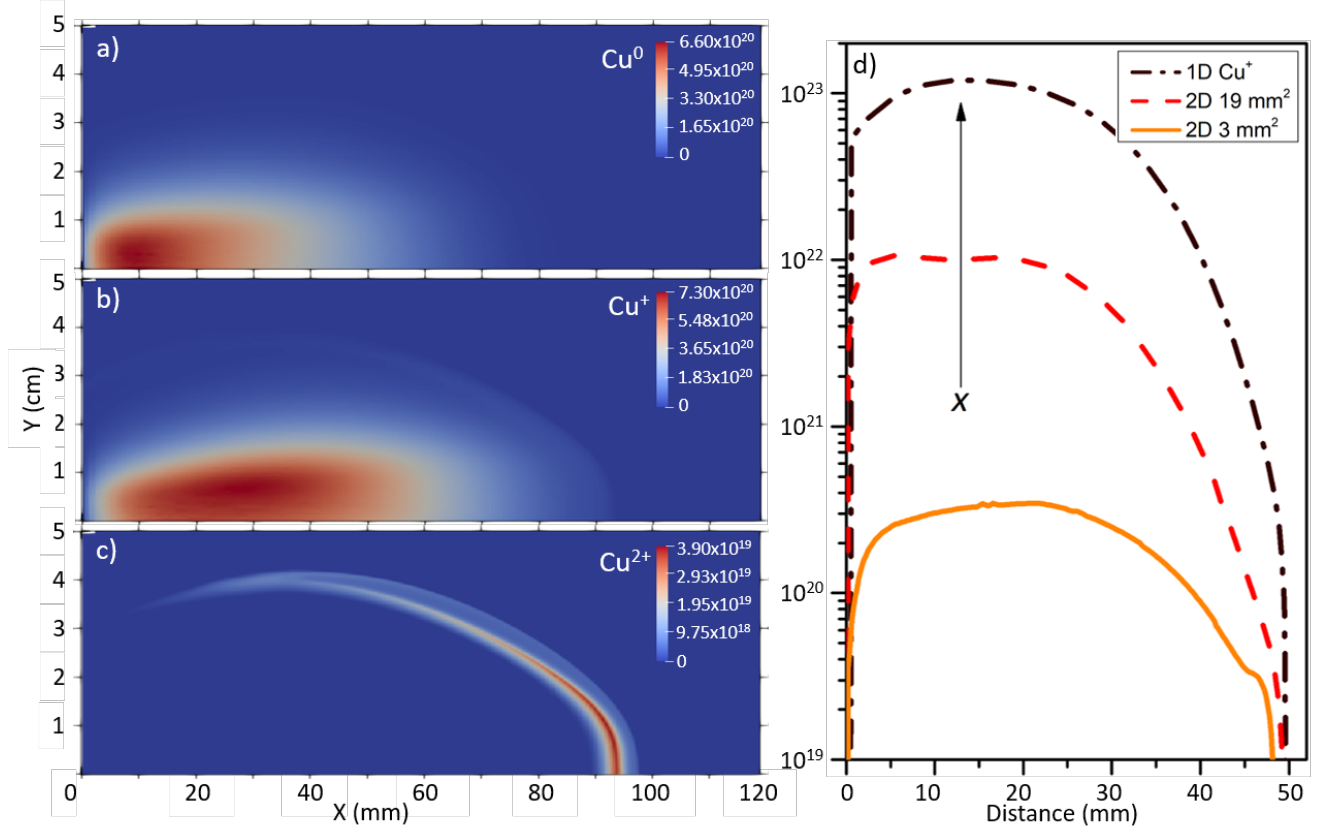


Figure 7: Results from the 2D-axisymmetric laser plasma simulation for a Cu target irradiated with 1×10^9 W/cm². The density is mapped for a) Cu⁰, b) Cu⁺, and c) Cu²⁺ for the case with a 19 mm² spot size, out to a distance of 100 mm. The species are spatially separated, with Cu²⁺ at the leading edge, Cu⁺ composes the main body of the plume, and Cu⁰ trailing behind. d) Comparison of the 1D simulated Cu⁺ density with the 2D using a large spot size and a small spot size (large and small x). The arrow indicates the direction of increase in the experimental parameter x . The 1D result overestimates the density when compared to the 2D simulations. Comparing the 2D results for large and small x , there is a difference of $\sim 10^2$ which is consistent with experiment.

never true in PLD. In the present work, the same 1D model has been extended to a 2D-axisymmetric implementation. The multidimensional simulation should capture the effects of the laser spot size and provide more quantitatively accurate results at long distances from the target.

The results of the 2D-axisymmetric simulation with two different spot sizes are compared to an identical 1D version and are summarized in Fig. 7. The spot sizes used were 19 mm² and 3.5 mm², which match the upper and lower bounds of the experimental values. Fig. 7a-c shows the density of Cu⁰, Cu⁺, and Cu²⁺, respectively, for the case of a 19 mm² laser spot with irradiance of 1×10^9 W/cm² (20 J/cm²) with a background pressure of 3×10^{-5} Torr. These values were chosen because similar conditions are used in the bulk of other laser-ablation simulations and will allow straightforward comparison. Even though the irradiance and background pressure are usually lower for PLD, the qualitative differences observed from changing the spot size will be the same. Ultimately, the plume expanded out to 20 cm in $7.9 \mu\text{s}$ but only the first 10 cm are shown in Fig. 7a-c. A point of interest is the spatial separation of charge species, with Cu²⁺ only at the leading edge, followed by the main body of Cu⁺, with the majority of the Cu⁰ far behind with much lower kinetic energy. This matches with the experimentally observed

behavior that the charged species are accelerated by the leading, ambipolar field. Also, the well known “forward peaking” of the plume is captured. Both of which are indicators that the simulation is behaving in a realistic manner. Each 2D simulation produced a plume whose leading edge reached 55 mm (the distance used in the experiments) at different times, indicating different kinetic energies between the two scenarios.

The difference in the kinetic energy and the density of the plume as the spot size is changed qualitatively matches the FeSe experiments. With the 19 mm² spot size, the first ions to reach 55 mm have a kinetic energy of 443 eV while the ions from the 3.5 mm² spot are slower, with kinetic energy of 291 eV. These values are consistent with many experiments done at this fluence [35]. This information is equivalent to the high energy “cut-off” in Fig. 5 and matches qualitatively with experiment, considering that the much higher laser fluence used in the simulation is expected to result in generally higher kinetic energies. In Fig. 7d, the density of Cu⁺ is plotted on the central axis for the 2D simulations, alongside a 1D version with identical parameters. The density is plotted out to an expansion distance of 50 mm for comparison, since that was the maximum of the 1D computational domain. The arrow in Fig. 7d indicates the direction of increase in the experimental parameter x . Recall

from experiments, the maximum value for $x = 1$ corresponds to a 19.3 mm^2 spot and the minimum $x = 0.18$ was a 3.5 mm^2 spot. The measured ion density decreased by a factor of 100 for any fixed fluence when reducing x from 1 to 0.18. The simulation clearly matches this result. The 1D case overestimates the density, as expected, when compared to 2D-axisymmetric simulations. Optimization of the 2D code for lower plasma density and laser irradiance is currently underway within our group and will be compared with matching experiments in a future study.

6. Conclusion

The properties of the laser-produced plasma will provide the key “experimental knob” required to achieve successful growth of FeSe monolayers with PLD. We have shown that the parameters of the plasma produced during ablation of FeSe can be fine-tuned over a wide range by choosing different combinations of laser fluence and spot size. When the laser fluence is held constant, reducing the beam spot/energy on the target can reduce the plasma density by 2 orders of magnitude. As such, the properties of the plasma could be kept constant while changing the ion kinetic energy, growth rate, or other conditions during growth of monolayers or heterostructures. The most important parameters for film growth, density and kinetic energy, can be tuned independently. Since density is correlated with film growth mode, it is possible to choose a desired growth mode and tune the kinetic energy distribution or vice versa. With low kinetic energy and low density, MBE-like growth of large grained monolayers should be possible in a high vacuum environment. The added benefit of tuning the kinetic energy of the particles provides more opportunities to control the growth process. Finally, we demonstrated that 1D simulations of laser-produced plasmas cannot capture these effects. To solve this problem, we introduced a 2D-axisymmetric simulation that enables computational study with various spot sizes.

Acknowledgments

This work was supported in part by the National Science Foundation (NSF) EPSCoR RII-Track-1 Cooperative Agreement OIA-1655280 and by a grant of high performance computing resources and technical support from the Alabama Supercomputer Authority (ASA). SBH acknowledges graduate fellowship support from the National Aeronautics and Space Administration (NASA) Alabama Space Grant Consortium (ASGC) under award NNX15AJ18H. RRA was partially supported by the Department of Energy (DOE) SBIR Project desc0015746. Any opinions, findings, and conclusions or recommendations expressed in this material are those of the authors and do not necessarily reflect the views of NSF, ASA, NASA or DOE.

References

[1] Q. Y. Wang, Z. Li, W. H. Zhang, Z. C. Zhang, J. S. Zhang, W. Li, D. Hao, Y. B. Ou, P. Deng, K. Chang, et al., *Chin. Phys. Lett.* **29**, 037402 (2012).

[2] Q. Song, T. L. Yu, X. Lou, B. P. Xie, H. C. Xu, C. H. P. Wen, Q. Yao, S. Y. Zhang, X. T. Zhu, J. D. Guo, et al., *Nat. Commun.* **10**, 758 (2019).
 [3] S. Shimizu, J. Shioagai, N. Takemori, S. Sakai, H. Ikeda, R. Arita, T. Nojima, A. Tsukazaki, and Y. Iwasa, *Nat. Commun.* **10**, 825 (2019).
 [4] J. Shioagai, Y. Ito, T. Mitsuhashi, T. Nojima, and A. Tsukazaki, *Nat. Phys.* **12**, 42 (2016).
 [5] D. N. Basov, R. D. Averitt, and D. Hsieh, *Nat. Mater.* **16**, 1077 (2017).
 [6] Z. Feng, J. Yuan, J. Li, X. Wu, H. W., B. Shen, M. Qin, L. Zhao, B. Zhu, V. Stanev, et al., arXiv: 1807.01273 (2019).
 [7] S. B. Harris and R. P. Camata, *J. Cryst. Growth* **514**, 54 (2019).
 [8] Z. Feng, J. Yuan, G. He, W. Hu, Z. Lin, D. Li, X. Jiang, Y. Huang, N. S., L. J., et al., *Sci. Rep.* **8**, 4039 (2018).
 [9] H. Hiramatsu, H. Sato, T. Katase, T. Kamiya, and H. Hosono, *Appl. Phys. Lett.* **104**, 172602 (2014).
 [10] H. Kim, R. P. Camata, S. Lee, G. S. Rohrer, A. D. Rollett, and Y. K. Vohra, *Acta Mater.* **55**, 131 (2007).
 [11] L. Iglesias, A. Sarantopoulos, C. Magén, and F. Rivadulla, *Phys. Rev. B* **95**, 165138 (2017).
 [12] A. Sarantopoulos, E. Ferreiro-Vila, V. Pardo, C. Magén, M. H. Aguirre, and F. Rivadulla, *Phys. Rev. Lett.* **115**, 166801 (2015).
 [13] H. N. Lee, S. Ambrose-Seo, W. S. Choi, and C. M. Rouleau, *Sci. Rep.* **6**, 19941 (2016).
 [14] M. Mahjour-Samani, R. Gresback, M. Tian, K. Wang, A. A. Puzos, C. M. Rouleau, G. Eres, I. N. Ivanov, K. Xiao, M. A. McGuire, et al., *Adv. Funct. Mater.* **24**, 6365 (2014).
 [15] S. Coh, D.-H. Lee, S. G. Louie, and M. L. Cohen, *Phys. Rev. B* **93**, 245138 (2016).
 [16] I. Weaver, G. Martin, W. Graham, T. Morrow, and C. Lewis, *Rev. Sci. Instrum.* **70**, 1801 (1999).
 [17] S. Metev, in *Pulsed Laser Deposition of Thin Films*, edited by D. Chrisey and G. Hubler (Wiley-Interscience, New York, 1994), pp. 255–264.
 [18] R. L. Merlino, *Am. J. Phys.* **75**, 1078 (2007).
 [19] B. E. Cherrington, *Plasma Chem. Plasma P.* **2**, 113 (1982).
 [20] H. M. Mott-Smith and I. Langmuir, *Phys. Rev.* **28**, 727 (1926).
 [21] F. F. Chen, *Phys. Plasmas* **8**, 3029 (2001).
 [22] F. F. Chen, *Plasma Sources Sci. T.* **18**, 035012 (2009).
 [23] B. Toftman, J. Schou, T. Hansen, and J. Lunney, *Phys. Rev. Lett.* **17**, 3998 (2000).
 [24] B. Doggett and J. Lunney, *J. Appl. Phys.* **105**, 033306 (2009).
 [25] D. Geohegan, in *Pulsed Laser Deposition of Thin Films*, edited by D. Chrisey and G. Hubler (Wiley-Interscience, New York, 1994), pp. 115–163.
 [26] S. I. Anisimov, B. Luk'yanchuk, and A. Luches, *Appl. Surf. Sci.* **96-98**, 24 (1996).
 [27] R. F. Wood, J. N. Leboeuf, K. Chen, D. Geohegan, and A. A. Puzos, *Appl. Surf. Sci.* **127-129**, 151 (1998).
 [28] T. N. Hansen, J. Schou, and J. G. Lunney, *Appl. Phys. A* **69**, S601 (1999).
 [29] Y. Franghiadakis, C. Fotakis, and P. Tzanetakis, *Appl. Phys. A* **68**, 391 (1999).
 [30] S. Amoroso, V. Berardi, R. Bruzzese, N. Spinelli, and X. Wang, *Appl. Surf. Sci.* **127-129**, 953 (2019).
 [31] J. Grun, R. Stellingwerf, and B. H. Ripin, *Phys. Fluids* **29**, 3390 (1986).
 [32] S. S. Harilal, *J. Appl. Phys.* **102**, 123306 (2007).
 [33] G. Hairapetian and R. I. Stenzel, *Phys. Fluids B* **3**, 899 (1991).
 [34] S. B. Harris, J. H. Paiste, T. J. Holdsworth, R. R. Arslanbekov, and R. P. Camata, *J. Phys. D Appl. Phys.* **53**, 015203 (2019).
 [35] X. Wang, S. Zhang, X. Cheng, E. Zhu, W. Hang, and B. Huang, *Spectrochim. Acta B* **99**, 101 (2014).